RESEARCH ARTICLE

NANO · MICRO small
www.small-journal.com

Multiphoton Lithography of Interpenetrating Polymer Networks for Tailored Microstructure Thermal and Micromechanical Properties

*Dorothee Silbernagl, Paulina Szymoniak, Zeynab Tavasolyzadeh, Heinz Sturm, and Ievgeniia Topolniak**

Multiphoton lithography (MPL), an emerging truly 3D microfabrication technique, exhibits substantial potential in biomedical applications, including drug delivery and tissue engineering. Fabricated micro-objects are often expected to undergo shape morphing or bending of the entire structure or its parts. Furthermore, ensuring precise property tuning is detrimental to the realization of the functionality of MPL microstructures. Herein, novel MPL materials based on interpenetrating polymer networks (IPNs) are presented that effectively combine the advantages of acrylate and epoxy systems. IPNs with varying component ratios are investigated for their microfabrication performance and structural integrity with respect to thermal and micromechanical properties. A variety of high-resolution techniques is applied to comprehensively evaluate IPN properties at the bulk, micron, and segmental levels. This study shows that the MPL laser scanning velocity and power, photoinitiator content, and multi-step exposure can be used to tune the morphology and properties of the IPN. As a result, a library of 3D MPL IPN microstructures with high 3D structural stability and tailored thermal and micromechanical properties is achieved. New IPN microstructures with Young's moduli of 3–4 MPa demonstrate high-to-fully elastic responses to deformations, making them promising for applications in morphable microsystems, soft micro-robotics, and cell engineering.

1. Introduction

Multiphoton lithography (MPL) has recently attracted significant research interest as it has emerged as one of the most outstanding processing techniques to create high-resolution, full 3D mesoscale to submicron structures.[1] This additive manufacturing technology applies tightly-focused femtosecond laser pulses to initiate the polymerization, which occurs only in the volume pixel, called the voxel. Here, the photon density in the focal area exceeds TW cm^{-3}, thereby crossing the polymerization threshold. By moving the focal spot through the monomer volume, 3D structures with full freedom of geometry can be assembled. Addressing the concept of miniaturization, MPL fabrication found application in the field of biomedicine,[2–5] micro-robotics.[6,7] micro-/nano-photonics,[8,9] micro-optics,[10–12] micro-fluidics,[13,14] micro-mechanical systems.[15,16] and plasmonic and metamaterials.[17,18]

While there are various photoresist formulations used for MPL 3D fabrication, each with its own set of properties, finding the ideal material for a specific application can be challenging. Consequently, there is a pressing need to expand the range of materials compatible with MPL technology. Most of the negative photoresists used in MPL are either acrylate- or epoxide-based due to their high curing efficiency, suitable optical properties, high structural resolution, and stability resulting from mechanical strength.[19]

A prominent feature of acrylate polymerization is its rapid kinetics, which is essential for the successful "writing" of 3D microstructures at laser scanning velocities of 10 000 µm s^{-1} and higher. However, rapid crosslinking usually results in the formation of internal stresses and low crosslinking degrees due to the steric hinderance of acrylate groups from reaching each other in a sudden frozen confirmation of the partially reacted monomers.[20,21]

On the other hand, epoxide-based photoresists, which undergo less reactive, cationic photopolymerization, exhibit several advantages such as no oxygen inhibition, low shrinkage, good adhesion to a vast range of substrates, and post-exposure polymerization processes, also known as dark polymerization.[22] The latter phenomenon can be characterized by slow crosslinking processes that allow the monomer molecules to reorganize into the system with minimized internal stress. Thus, epoxide-based systems can be used as additives to reduce the brittleness of the acrylate-based materials, creating an interpenetrated phase that is slowly polymerized during and after exposure, during the dark-curing stage.

D. Silbernagl, P. Szymoniak, Z. Tavasolyzadeh, H. Sturm, I. Topolniak
BAM Bundesanstalt für Materialforschung und -prüfung
Unter den Eichen 87, 12205 Berlin, Germany
E-mail: ievgeniia.topolniak@bam.de

The ORCID identification number(s) for the author(s) of this article can be found under https://doi.org/10.1002/smll.202310580

DOI: 10.1002/smll.202310580

This results in the formation of interpenetrating polymer network (IPN) materials.

IPN are materials that consist of at least two chemically distinct networks that are at least partially interlaced and, in theory, are not covalently bonded to each other.[23] Most IPNs do not interpenetrate at the molecular level and are typically composed of finely divided phases that are about tens of nanometers in size.[24] Since IPNs contain two or more different polymeric structures with different chemical functionalities, these hybrid materials exhibit tunable properties resulting from the physicochemical nature of each component and the degree of phase separation of the formed polymers, which are immiscible with each other. The appealing aspects of IPN conferred their use in biomedical and optical applications, for drug delivery and tissue engineering, gas absorption, sound and vibration damping, as adhesives, and much more.[25] We believe that the combination of the high precision and design freedom inherent in MPL fabrication with the ease of tuning the properties of IPN materials will enable the development of novel functional microdevices and advance applications in micro-robotics, biomimetics, and tissue engineering.

The integrity of MPL microstructures or their ability to comply to external stimuli is essential. Therefore, tailoring the thermal and mechanical properties of fabricated 3D IPN objects for a specific application, to the best of our knowledge, received little to no attention and remains the subject of extensive ongoing research. To date, a better understanding of the underlying phenomena and mechanisms that determine the performance of the structure would unravel the fabrication strategy predetermined by the targeted application. However, highly sensitive space-resolved methods are essential to address this challenging task.

One of the critical properties of polymers that determines their end-use potential and operation is the glass transition, characterized by the glass transition temperature (T_g). It is commonly investigated by conventional differential scanning calorimetry (DSC), which is an impractical tool for MPL structures due to their dimensions being in micro- or nanoscale. A novel fast scanning calorimetry (FSC) technique is a great alternative to study the thermal behavior of 3D microstructures with a sample mass in the submicron range.[26]

Given the dimensions of the 3D micro-object fabricated by MPL, methods of atomic force microscopy force spectroscopy, particularly AFM force-distance curve (FDC), has gained popularity to determine material properties at microscale. This technique has been also used to characterize MPL microstructures, mostly to analyze MPL structures topography and Young's moduli.[27–29] However, intermodulation AFM mode (ImAFM) is essential for targeting exceptional resolution to determine mechanical properties on sub-micron range.[30,31] This technique holds great promise for understanding the behavior of IPN materials.

In this work, we present new epoxy-acrylate IPN dual-cure materials structured by means of Multiphoton Lithography. Combining the advantages of two different photocuring mechanisms, radical and cationic, we aim at 3D microstructures whose properties can be tailored by varying the component ratio and the MPL fabrication parameters. The studied mixtures consist of polyethylene glycol diacrylate (PEGDA) and cycloaliphatic epoxide functional groups. Consequently, cyclopentanone-based photoinitiator, and triarylsulfonium hexafluorophosphate salt were used to ensure cationic and radical polymerization, respectively. We evaluated the MPL fabrication integrity of the IPNs and investigated the selected IPN microstructures for their thermal and micro-mechanical properties by means of fast scanning calorimetry, force-distance curve AFM, and intermodulation AFM. This unique combination of highly sensitive space-resolved methods allows us to gather information on MPL IPN microstructures from the bulk to the micron to the segment level. We obtained, for the first time, the glass transition temperature and fragility factor from thermal behavior of the MPL microstructure and investigated its behavior with respect to laser scanning velocity, intensity, photoinitiator concentration and multi-step exposure. Furthermore, the elastic-plastic behavior of the microarchitectures was evaluated in terms of IPN morphology at micrometer and sub-micrometer range. The fabricated 3D IPN microstructures exhibit higher structural strength and integrity compared to PEGDA. At the same time, the IPNs with 1 wt.% of photoinitiator exhibit high to fully elastic recovery (up to 100%), with the Young's moduli of bulk structures ≈3–4 MPa. These characteristics position IPNs as a good base material for the modelling microstructures with intricate 3D designs for biomimetics and scaffold engineering. In addition, our funding encourages further development and exploration of IPN systems as versatile and easily tunable materials for 3D MPL microstructuring.

2. Results and Discussion

Photoresists based on polyethylene glycol diacrylate and its mixtures with cycloaliphatic epoxide, namely, 3,4-epoxycyclohexylmethyl-3′,4′-epoxycyclohexane carboxylate (ECC) were tested for their performance at fabricating precise 3D microstructures with MPL technique. Next, the morphology, thermal and mechanical properties of selected candidates were characterized with FSC, AFM FDC, and ImAFM techniques. While FSC and AFM FDC mapping is used to determine the thermal and mechanical properties, respectively, of the entire microstructure, single FDC probing and ImAFM techniques provides information on the local mechanical response of the material at the micron and sub-micron level resolutions. It should be noted that from thermal observations, mechanical properties cannot be directly deduced due to the nature and organizational levels of the material.

2.1. MPL Microstructuring

We investigated the fabrication window by creating PEGDA IWP[32] scaffold arrays with varying laser intensities and scanning velocities (**Figure 1**). It can be clearly seen that the laser intensity parameter has a major influence on the shape quality of the microstructures, with the fabrication window ranging between 2.2 and 12.9 TW cm^{-2} (5 and 30 mW). As the laser intensity increases, the structural quality of scaffolds improves. This can be attributed to the increase in the conversion degree of polymerization, which, in turn, affect various material properties.[33,34] However, at intensities ≈8.6 TW cm^{-2} and higher, the 3D structure starts to expand owing to the energy overload, which may result in secondary polymerization mechanisms.[35] Meanwhile, changing the laser velocity had no apparent effect on the IWP shape.

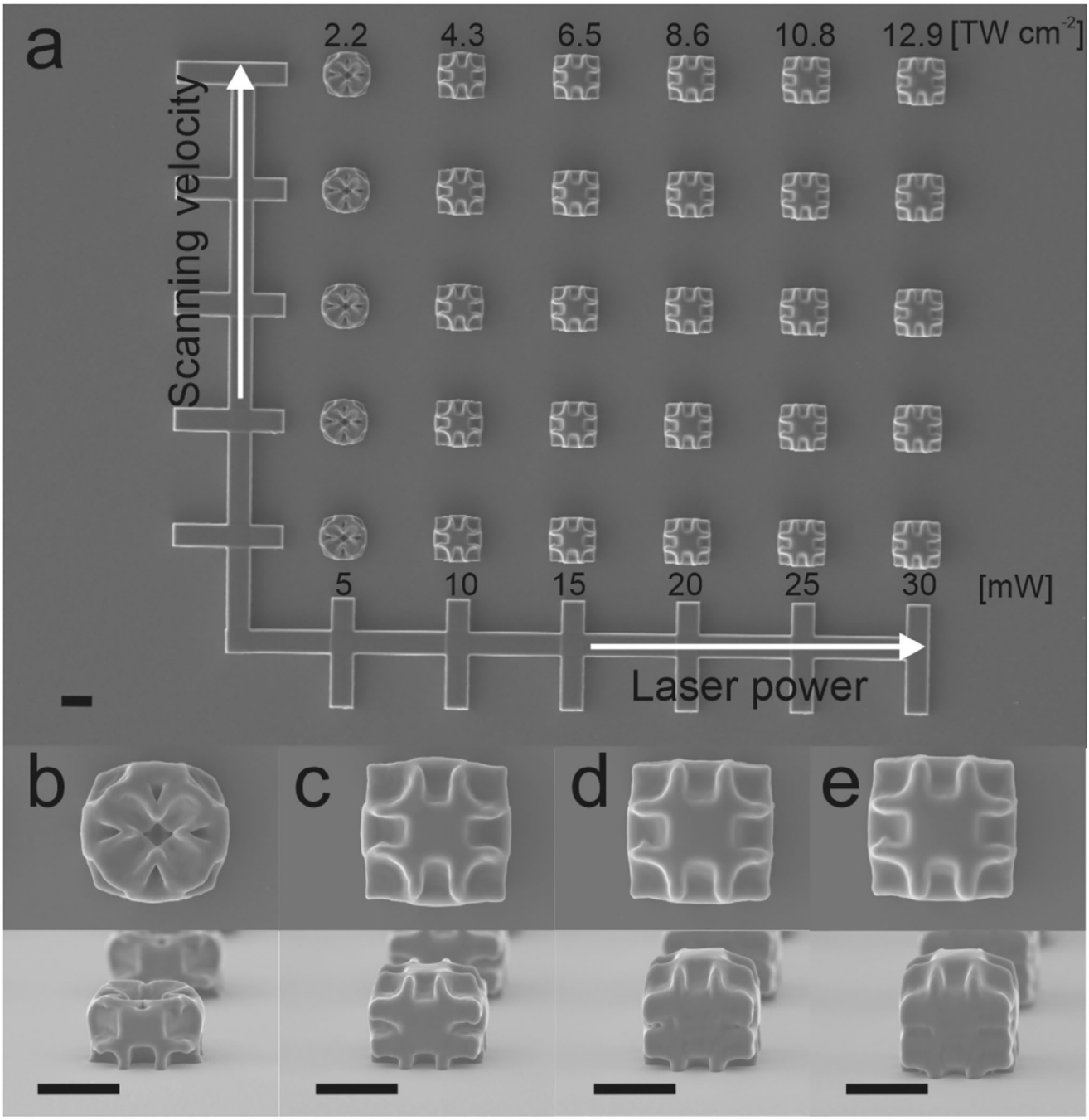

Figure 1. PEGDA microstructuring. SEM micrographs of PEGDA IWP scaffold units. a) calibration array in the 2.2–12.9 TW cm^{-2} and 1000–10 000 µm s^{-1} fabricated with 1.4 NA. Top and side view of the individual microstructures: b) 2.2 TW cm^{-2}, 10 000 µm s^{-1}; c) 4.3 TW cm^{-2}, 10 000 µm s^{-1}; d) 6.5 TW cm^{-2}, 10 000 µm s^{-1} and e) 8.6 TW cm^{-2}, 10 000 µm s^{-1}. All scale bars, 20 µm.

PEGDA shows good processability with respect to simple bulky microstructures such as IWP scaffold units. On the other hand, the cycloaliphatic epoxide ECC alone could hardly be microstructured, and only objects produced at 12.9 mW could be obtained (Figure S1, Supporting Information). Next, IPN with PEGDA and ECC weight ratios of 3:7, 1:1, and 7:3, respectively, were subjected to microstructuring. However, the PEGDA:ECC 3:7 system showed poor integrity and high levels of shrinkage (Figure S2, Supporting Information), indicating that excessive epoxide content led to the critical disruption of the acrylate network, which in turn resulted in low structural stability. In contrast, for the PEGDA:ECC 1:1 and 7:3 compositions, complex 3D microstructures were successfully obtained (**Figure 2**; Figure S3, Supporting Information).

Similar to pristine PEGDA, the IPN blends show a greater sensitivity to laser intensity rather than to scanning velocity. When

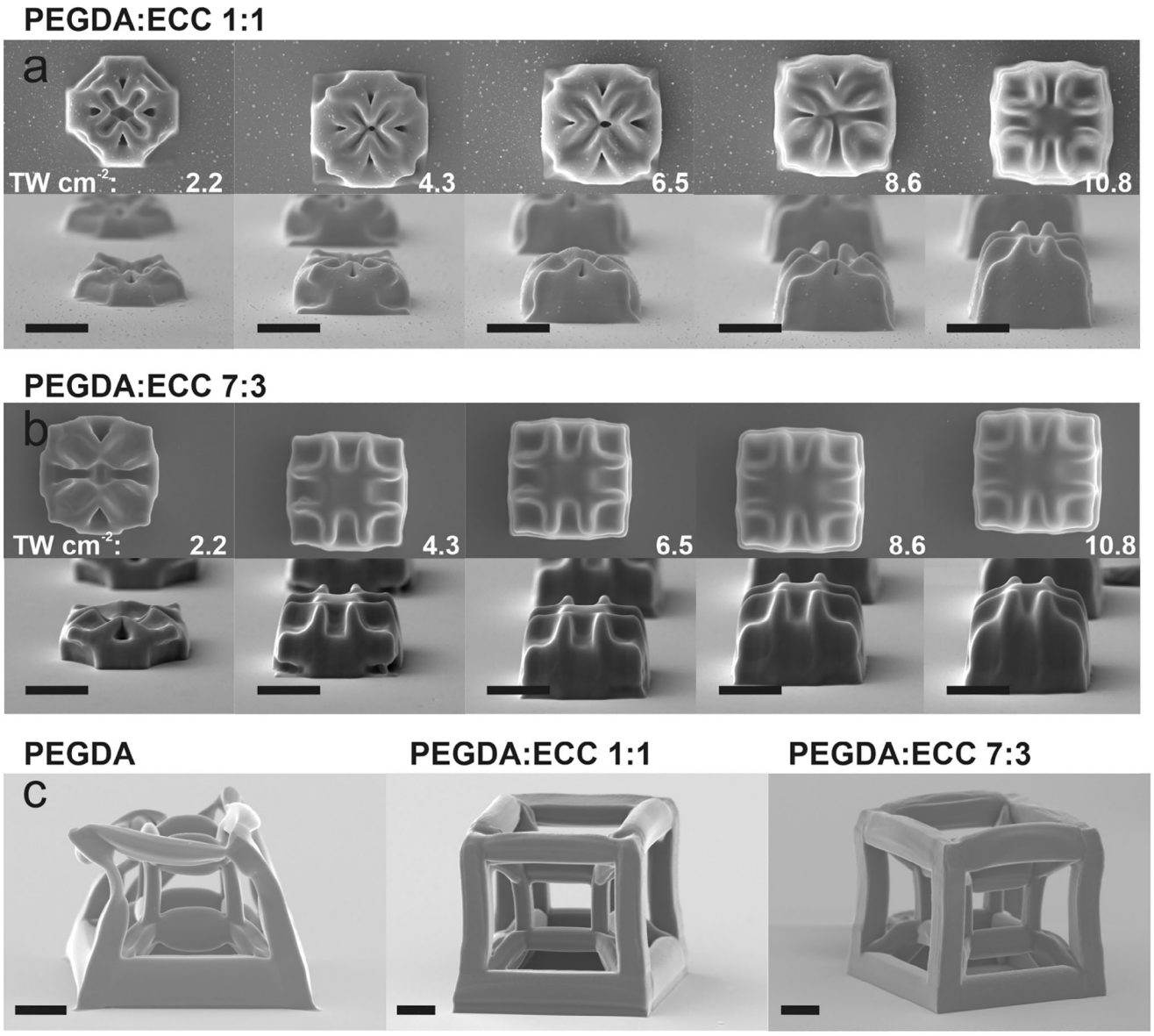

Figure 2. IPN microstructuring. SEM micrographs of PEGDA:ECC IWP arrays for: a) 1:1 and b) 7:3 component ratios. All structures were fabricated at 10 000 µm s^{-1} and laser intensities of 2.2, 4.3, 6.5, 8.6, 10.8 TW cm^{-2}. c) 3D hypercube structure of PEGDA (left), PEGDA:ECC1:1 (center), PEGDA:ECC 7:3 (right). All structures are fabricated at 8.6 TW cm^{-2} and 5000 µm s^{-1}. All scale bars, 20 µm.

equal amounts of both components are present (Figure 2a), the IPN exhibit signs of undercuring with a gradual improvement in structural stability as the laser intensity increases. However, the composition with a higher content of PEGDA shows no signs of undercuring at laser intensities ≥ 4.3 TW cm^{-2} (Figure 2b). The subsequent behavior is similar to that of the pristine PEGDA.

Surprisingly, obtaining structures with more intricate 3D designs, such as hypercubes, was not successful when pristine PEGDA was used, indicating insufficient structural stability of this viscoelastic hydrogel (Figure 2c, left). Compared with PEGDA, the PEGDA:ECC IPN formulations show better stability of the hollow 3D microstructure (Figure 2c, center, right). Therefore, we consider these IPN formulations as better alternatives to PEGDA to achieve complex 3D microstructure designs. Additional examples of IPN 3D scaffold microstructures are provided in Figure S4 (Supporting Information). The observed enhancement phenomenon and the effect of the fabrication parameters are investigated in greater detail in this work through a better understanding of the changes in the topography and the thermal and mechanical properties of the IPN microstructures.

2.2. Thermal Properties

The glass transitions of the pure PEGDA and PEGDA:ECC mixtures were investigated with fast differential scanning

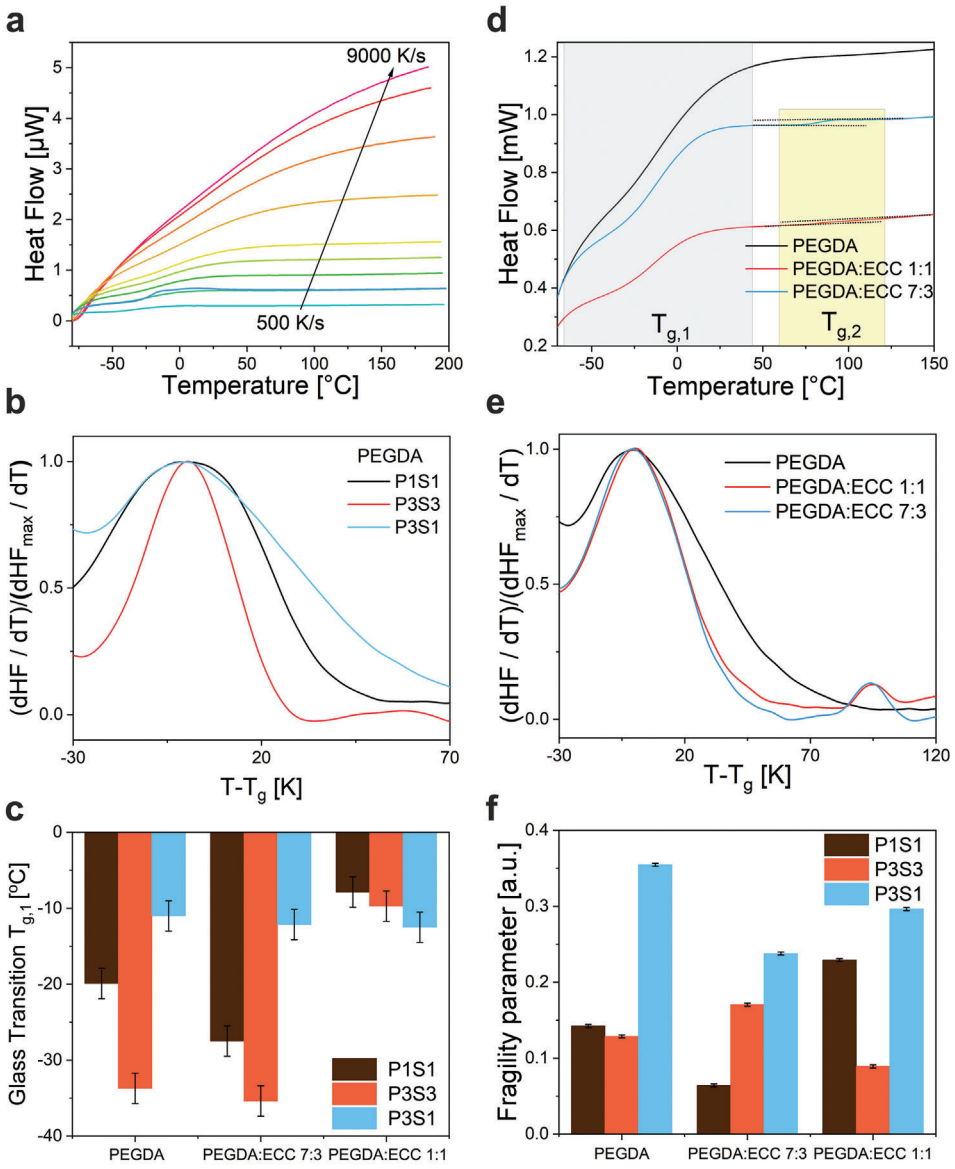

Figure 3. Thermal properties. a) Flash DSC heat flow curves for PEGDA microstructures fabricated at 20 mW (9.8 TW cm^{-2}) and 1000 µm s^{-1} (P3S1) for successive heating runs at indicated heating rates from 500 to 9000 K s^{-1}. b) Normalized derivative of the heat flow measured at 2000 K s^{-1} plotted versus temperature reduced by T_g for PEGDA structures fabricated at different conditions. c) Glass transition temperature of PEGDA and PEGDA:ECC blends obtained by fast scanning calorimetry at 2000 K s^{-1}. d) Heat flow curves for PEGDA and PEGDA:ECC blends microstructures. e) Normalized derivative of the heat flow measured at 2000 K s^{-1} plotted versus temperature reduced by T_g for PEGDA and blends. Samples in d) and e) are fabricated at 20 mW and 1000 µm s^{-1} (P3S1). f) Fragility parameter D calculated from activation plots.

calorimetry. We were able to fabricate the IPN microstructures directly on the FSC chip sensor membrane to ensure the integrity of the printed structures. To the best of our knowledge, this is the first study of using FSC to characterize MPL fabricated microstructures.

Based on the calibration experiment performed to define MPL fabrication window (Figures 1 and 2) we selected similar fabrication conditions: 10 mW (4.9 TW cm^{-2}), 1000 µm s^{-1}; 20 mW (9.8 TW cm^{-2}), 7000 µm s^{-1}; and 20 mW (9.8 TW cm^{-2}), 1000 µm s^{-1}. These parameters are further indicated as P1S1, P3S3, and P3S1, respectively (Table S1, Supporting Information). The glass transition depends on the applied scanning rate ($\dot{T}$), where for higher values of $\dot{T}$ the glass transition occurs at higher temperatures, as it is observed for heating curves of PEGDA in **Figure** 3a.

First, it was found that in the probed temperature range one glass transition region is observed for all PEGDA microstructures regardless of MPL fabrication parameters (Figure 3b). As shown in Figure S5 (Supporting Information), no thermal post-cure events, which are typically observed in the first heating run as broad exothermic features in the heat flow data, were observed.

Therefore, the as-prepared MPL microstructures can be considered as thermally stable.

The T_g values obtained for PEGDA and the blends under the same fabrication conditions are shown in Figure 3c and Table S1 (Supporting Information). For pristine PEGDA, T_g ranges from −33.7 °C to −11 °C. PEGDA is a linear polymer, which means that its T_g depends directly on the molecular weight, influenced by the degree of conversion achieved during polymerization. This indicates that the highest degree of polymerization exhibits microstructure printed with P3S1 parameters. Furthermore, the different T_g values obtained for PEGDA emphasize the significance of laser intensity and scanning velocity in the MPL process for tuning the photocuring process and material properties of the fabricated 3D micro-objects.

For PEGDA printed under P3S3 conditions, the narrow peak observed in Figure 3b indicates a narrow distribution of chain lengths, suggesting a more uniform molecular weight distribution. However, the peak becomes broader when the samples with lower scanning velocity, under P1S1 and P3S1 conditions are prepared. The resulting longer exposure time allows for the formation of longer chains during the propagation step, as also evidenced by the higher T_g values for P3S1 and P1S1, compared to P3S3. Nevertheless, lower scanning velocities also result in the formation of chains with lengths shorter and longer than the average, leading to increased heterogeneity in the system.

For IPN blends, the dependency is less straightforward and cannot be directly determined. Since IPNs are heterogeneous systems, one might expect two glass transition regions, related to vitrification of each component separately. Nevertheless, if upon the applied fabrication conditions one of the networks will have only low degree of conversion, whereas the other simultaneously has higher degree of conversion, only one glass transition might be detected related to the more polymerized system, as it is affected by blending and soft confinement.

Here, for both PEGDA:ECC 1:1 and 7:3 upon P1S1 and P3S3 fabrication, only one glass transition temperature is detected, which is found in the temperature range expected for pure PEGDA (see Figure 3d). In addition, no significant broadening is observed for the blend, compared to PEGDA (Figure 3e). This indicates that the ECC network did not achieve a degree of conversion high enough to be detected by fast scanning calorimetry. Therefore, the probed glass transition originates from PEGDA as it is influenced by ECC.

The increase of viscosity for the blends compared to pure PEGDA slows down the diffusion of active excited molecules toward monomers. Therefore, one would expect lower chain lengths for PEGDA in the blended systems, which might result in a significant decrease of the T_g values. However, for IPNs, the materials affect each other on the microscopic scale. The stiff crosslinked network of ECC introduces a spatial obstacle to the flexible PEGDA chain, acting as soft confinement. Consequently, the stiffness and T_g of the system increase for well-tuned compositions of IPNs. Thereupon, the obtained macroscopic structures with complex shapes will be more stable when flexible PEGDA is blended with stiffer ECC, as evidenced in Figure 2c.

Because photolysis is faster than photochemical reactions and mass transport, the T_g values are higher for slower scanning speeds at the same power. The increase of T_g in the blend compared to that of pure PEGDA is most apparent for the 1:1 composition ratio. For the P1S1 and P3S3 fabrication parameters the T_g is higher than for pure PEGDA. Here, on one hand, owing to the high viscosity of the mixture, the degree of conversion of PEGDA, and consequently the chain lengths, will be lower than that of pure PEGDA. Nevertheless, the flexible PEGDA chains are subjected to a confinement effect originating from the stiffer ECC scaffold, therefore affecting the mobility of PEGDA. Moreover, one should consider post-exposure polymerization processes that can appear for ECC as cationic polymerization is known to exhibit a dark curing process.[36]

For the 7:3 composition, the T_g decreases for P1S1 and P3S3, compared to PEGDA. The reason for this can be attributed to the fact that there is a substantially lower concentration of the ECC component in the 7:3 mixture compared to the 1:1 system. First, the 7:3 blend experiences the disadvantage of an increase in viscosity. Second, the soft confinement effect of ECC on PEGDA will be weaker for 7:3 mixture at these fabrication conditions.

Nonetheless, for both PEGDA:ECC 1:1 and 7:3 at high laser power and lower scanning speed (P3S1), an additional high-temperature glass transition, denoted as $T_{g,2}$, is detected ca. 96 °C (Figure 3d,e). As discussed above, the components in IPNs are not miscible at the molecular scale. In the given case, the presence of a second $T_{g,2}$ is related the sufficiently crosslinked ECC material, as it is found in a temperature range significantly higher than that for pure PEGDA. This can be also partial result of heat accumulation, which would be highest for P3S1 fabrication parameters. Presence of two T_g indicates that a well-developed interpenetrating network is formed.

Lastly, we compared the fragility parameter (D) for each material (details in Figure S6 and Table S2, Supporting Information) in Figure 3f. Here, D is considered only for the low temperature transition $T_{g,1}$, i.e., that of pure PEGDA and of PEGDA in blends as it is affected by ECC. For pristine PEGDA and the blends, the highest fragility parameter is observed for P3S1 conditions. In the case of pristine PEGDA it can be attributed to the highest conversion rate indicated by the highest T_g value and therefore can be correlated to an increase of chain length.[37] For the blends, the increase in fragility is not related to an increase in PEGDA chain lengths, but rather to a soft confinement of ECC on the mobility of PEGDA.

2.3. Mechanical Properties

Two AFM force spectroscopy methods were applied to study mechanical properties of the fabricated 3D objects: force-distance curves to study mechanical properties at the microscale,[38,39] and intermodulation AFM to investigate mechanical properties and bulk chemical composition of IPN at the submicron scale.[30,31]

The FDC evaluation (details in Supporting Information) yields the maximum deformation of the sample D_{max} at the maximum applied force F_{max} (Figures S7–S10, Supporting Information). The smaller the deformation D_{max}, the higher the apparent stiffness, and therefore, the resistance to deformation. To distinguish plastic and elastic ($D_{elastic}$) deformations, we determine the elastic recovery (1-($D_{elastic}$/D_{max}), Equations S4 and S5, Supporting Information) as an additional parameter. Elastic recovery quantifies the elasticity of the material, which is crucial for the shape stability of the microstructure. In general, high stiffness is associated

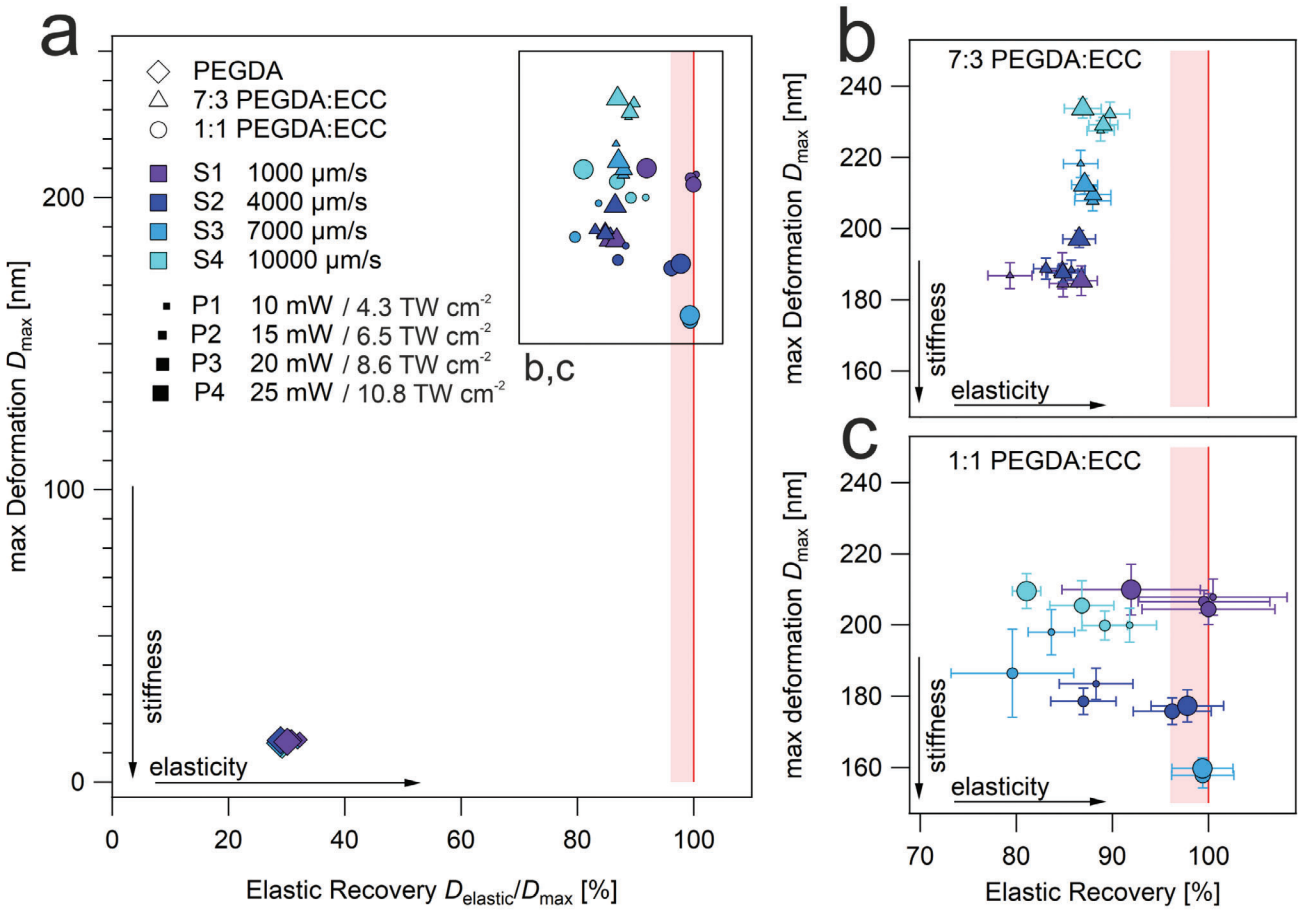

Figure 4. Viscoelastic properties. a) Maximum deformation of MPL fabricated PEGDA and PEGDA:ECC microstructures plotted versus sample elastic recovery with respect to different laser power and scanning velocity parameters. PEGDA is indicated as rhombus, PEGDA:ECC 7:3 as triangle, PEGDA:ECC 1:1 as circle; 16 samples fabricated with different combinations of laser powers and velocities are displayed by variations of data point sizes and colors as depicted in the figure. Resolved data points including measurement error are given for b) PEGDA:ECC 7:3 and c) PEGDA:ECC 1:1. Maximum elastic recovery of materials (>96%) is indicated by red area. Fully elastic behavior (elastic recovery 100%) is indicated by red line. Force-distance curves were recorded at 1 Hz and a maximum applied force of 68 nN.

with elasticity and low apparent stiffness is associated with plasticity. To correlate these two properties for pristine PEGDA, apparent stiffness (maximum deformation D_{max}) is plotted against elastic recovery in **Figure 4**.

Pristine PEGDA shows a higher resistance to deformation, indicated by a low D_{max} in the range between 10 and 20 nm (Figure 4; Figure S11, Supporting Information). Considering the low elastic recovery values of PEGDA, which are in the range of 28–33%, it is obvious, that the deformations in PEGDA are mostly plastic. This is a typical behavior for gels, which are more viscous than stiff. Consequently, such structures cannot recover their shape from even small deformations, which, in turn, can lead to low structural stability of the material, as shown in Figure 2c.

The stark difference in properties is evident when comparing the results of the pristine PEGDA samples with the IPN blends (Figure 4a). The maximum deformations D_{max} of PEGDA:ECC blends (Figure 4a, triangle and circle markers) are about ten times higher than those of the pristine PEGDA, ranging from 150 to 250 nm. An increase in D_{max} is usually associated with an increase in plastic deformation. However, this is not the case for PEGDA:ECC as the elastic recovery of this material reaches more than 80%, meaning that the material response is predominantly elastic. This results in better structural stability and resistance to permanent deformation of the IPN material and its 3D microstructures (Figure 2c).

A detailed examination of PEGDA:ECC 7:3 shows that the laser scanning velocity, indicated by different colors in Figure 4, is an important parameter influencing D_{max}. The outcomes align with the findings from thermal investigations (Section 2.2), which demonstrate that the laser scanning velocity impacts the molecular weight of PEGDA. At lower velocities, higher molecular weight PEGDA is more likely to form. Consequently, as the scanning velocity decreases, D_{max} becomes smaller, and the material exhibits greater resistance to deformation, closely resembling the properties of pure PEGDA. However, the dependence of the mechanical properties on the fabrication parameters for PEGDA:ECC 1:1 is not as clear (Figure 4c), indicating the presence of an additional effect on the growth of the epoxide and PEGDA networks.

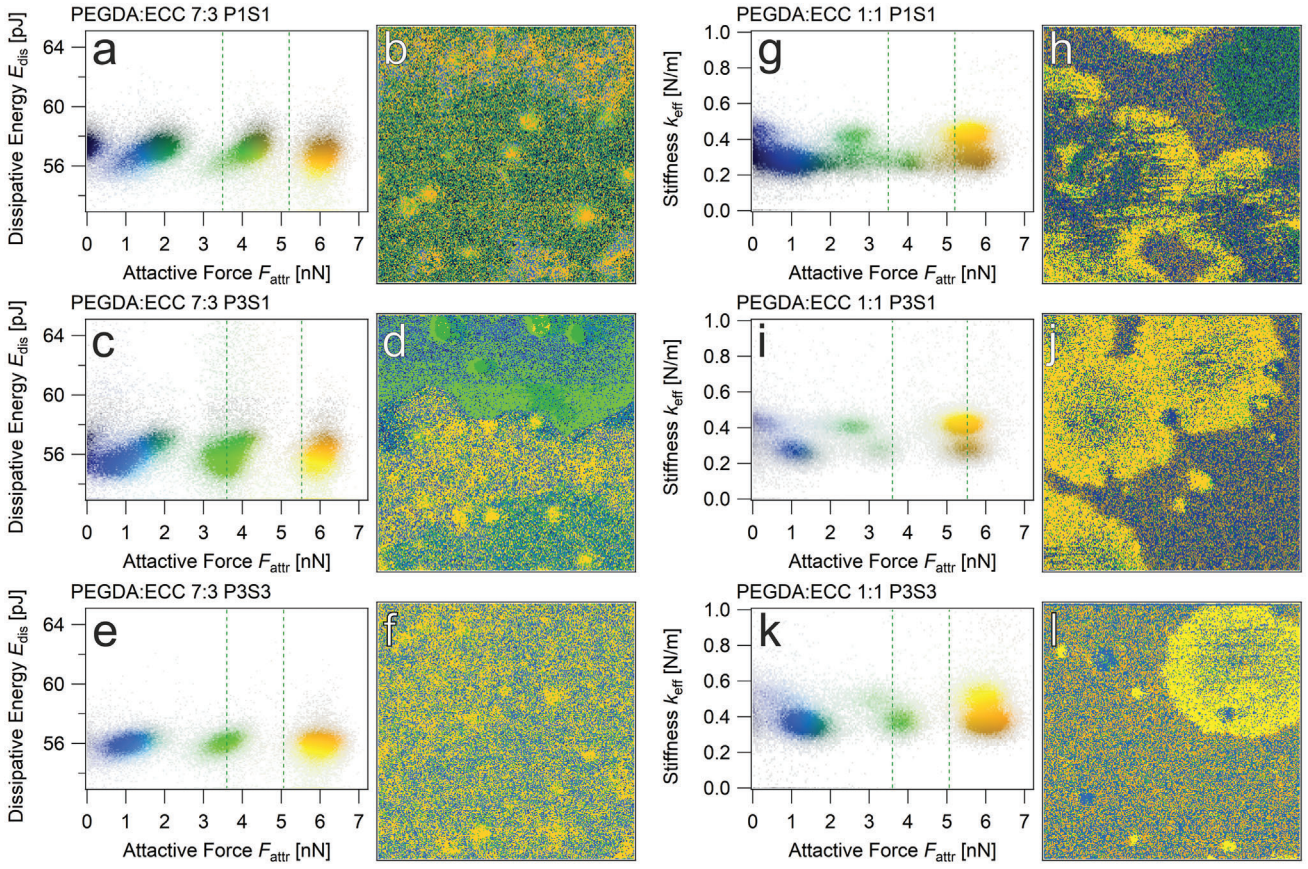

Figure 5. Phase distribution in IPN. a,c,e) Heatmaps of PEGDA:ECC 7:3 samples fabricated at 10 mW (4.3 TW cm^{-2}), 1000 µm s^{-1} (P1S1); 20 mW (8.6 TW cm^{-2}), 7000 µm s^{-1} (P3S1) and 20 mW (8.6 TW cm^{-2}), 1000 µm s^{-1} (P3S3). b,d,f) Corresponding 2 × 2 µm^2 spatial domains based on heatmap color scale. g,i,k) Heatmaps and h,j,l) Corresponding spatial domains of PEGDA:ECC 1:1. Colors in the heatmaps are based on the scalebar given in Figure S19 (Supporting Information). Stiffness k_{eff} and dissipative energy E_{dis} are scaled as a function of brightness. Material phases, represented by attractive force F_{attr}, are presented by F_{attr} value in blue–green–orange color range. For comparison, the green dotted lines in the heatmaps indicate the limits of the PEGDA cluster Gaussian distribution at half height under the same fabrication parameters.

Importantly, even higher elastic recovery values are detected for PEGDA:ECC 1:1, in some cases reaching the optimum value of 100% (Figure 4c, red line), where the deformations are fully elastic. Compliance in organic materials is based on large free volume and weak interactions such as hydrogen bonding and van der Waals interactions. Therefore, compliant or soft materials are usually expected to yield and deform plastically under stress. In our case, we were able to achieve highly compliant IPN samples with a Young's moduli in the range of 3–4 MPa (Table S3, Supporting Information, fit with Hertz theory: see Figure S10 and Equations S6 and S7, Supporting Information) that behave perfectly elastic. This is particularly rare considering the presence of PEGDA in the IPN composition. This uncommon phenomenon gives us the opportunity to design intricate 3D structures that do not yield from surface tension or other stresses and maintain their shape, analogous to a spring.

It appears that to achieve an elastic recovery of more than 96% in IPN 1:1, a certain light dose per unit of time is required. This can be achieved either by reducing the scanning velocity or by increasing the laser power. In our experiment, we were able to obtain fully elastic materials with a PEGDA:ECC ratio of 1:1 using the following parameters: 10–20 mW at 1000 µm s^{-1} and 20–25 mW at 7000 µm s^{-1} with D_{max} of 204–208 nm and 158–160 nm, respectively (Figure 4c).

For a deeper elucidation of the underlying mechanisms influencing the observed mechanical properties of the IPN structures, we have chosen an additional method of force spectroscopy, ImAFM with the equivalent of FDC, amplitude dependent force spectroscopy (ADFS). This method has a much higher lateral resolution than FDC, and thus allows to study the morphologies of IPN structures at the nanoscopic scale. The topographies of areas selected for ImAFM are given in Figures S12–S14 (Supporting Information).

For a structure-property correlation the stiffness k_{eff} in the case of PEGDA:ECC 7:3 and the dissipative energy E_{dis} in case of PEGDA:ECC 1:1 were correlated with the attractive force F_{attr} that is specific to the chemical composition.[40] (**Figure 5**, left plots). Details on ImAFM and spatial domain of each channel are provided in Supporting Information and Figures S15–S17 (Supporting Information). From the 2D heatmaps a cluster analysis (double Gaussian) was performed which resulted in false-color maps of the spatial domain (Figure 5, right plots).

The maximum attractive force F_{attr} (Figures 5a,c,e and 1D histograms are in Figure S18, Supporting Information) shows at

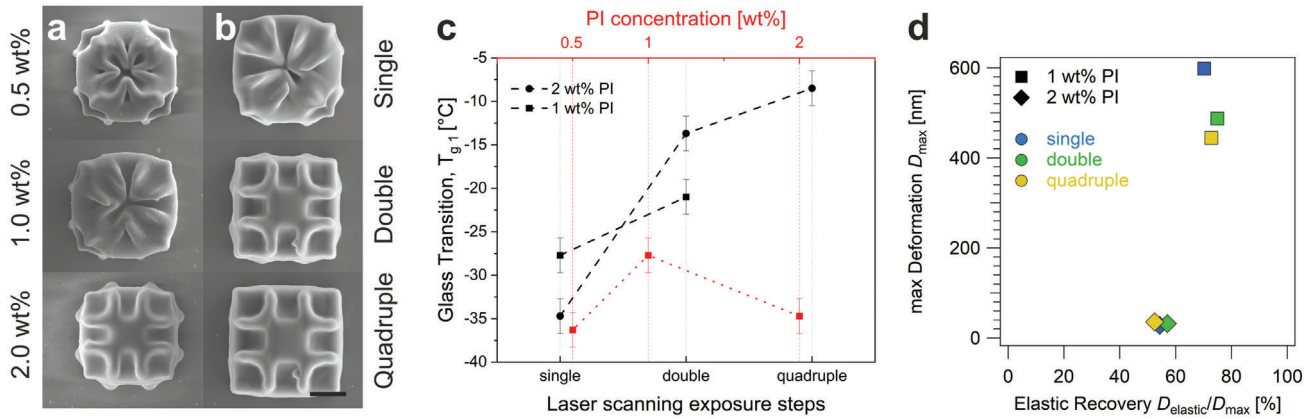

Figure 6. Multiple laser exposure and photoinitiator concentration. SEM micrographs of PEGDA:ECC 1: 1 IWP scaffold unit fabricated at 6.5 TW cm^{-2}. a) IWP units fabricated with 0.5, 1.0 and 2.0 wt.% of each, radical and cationic photoinitiator. b) IWP units fabricated in a single-, double-, and quadruple-step laser scanning exposure process. All scale bars, 5 µm. c) Dependency of first glass transition and d) maximum deformation versus elastic recovery on the number of steps in multi-step laser scanning. Samples for (c) and (d) were PEGDA:ECC 1:1 fabricated at 4.9 TW cm^{-2}, 7000 µm s^{-1}.

least three distinct material phases in all IPNs. The middle peak is assigned to a PEGDA-rich network (IPN$_P$, 2–2.5 pJ < F_{attr} <5 pJ) as this is very similar to values obtained for pristine PEGDA. The high value peak is assigned to an ECC-rich network (IPN$_E$, F_{attr} > 5 pJ), due to its higher refractive index than that of PEGDA.[41,42] A weakly attractive phase detected in the region below 2.5 pJ is assigned to a lower density material (IPN$_U$, F_{attr} < 2–2.5 pJ). This may be due to immiscibility or low molecular weight fragments. Therefore, we suspect undercured or stochastically / sterically disturbed networks.

In general, for PEGDA:ECC 7:3 and 1:1 fabricated at lower laser powers (Figure 5a,c,g,i), one observes that the material appears to be partially undercured, since IPN$_U$ is present. It is also noteworthy, that all three networks, IPN$_P$ and IPN$_E$ and IPN$_D$, contribute to the bimodal distribution of mechanical properties (E_{dis} and k_{eff}). This is due to soft confinement, as both networks are mechanically intertwined to a degree, that their separate mechanical properties cannot be resolved, even at the resolution presented.

The 2D histograms of PEGDA:ECC 7:3 (Figure 5a,c,e) show that with increasing power, the dissipative energy E_{dis} decreases for ≈2 pJ, meaning that the material response becomes more elastic. Moreover, the spatial domains indicate that the lower fabrication velocity (Figure 5b,d; Figure S13, Supporting Information) results in a PEGDA-rich region where the ECC is depleted with a phase separation appearing visible along to the laser scanning motion (along to the x-axis). This confirms that lower scanning velocity are beneficial for the development of the PEGDA network, but at the expense of the ECC network. On the other hand, at a faster fabrication speed, PEGDA and ECC are homogeneously distributed (Figure 5f).

For PEGDA:ECC 1:1 (Figure 5g,i,k) the k_{eff} increases slightly with increasing power. In the spatial domain of PEGDA:ECC 1:1 (Figure 5h,j,l), the spherulitic features, which we believe are a result of spinodal phase separation phenomenon.[24] (see Figure S20, Supporting Information), become visible as an ECC-rich phase that can develop relatively undisturbed from PEGDA. These morphological patterns are also observed on the phase images obtained at AFM tapping mode (Figure S14, Supporting Information). These spherulitic ECC-rich phases are the main difference between the PEGDA:ECC 7:3 and PEGDA:ECC 1:1 materials. From this we conclude that this is the main reason for the superior elasticity of PEGDA:ECC 1:1 observed at the micron level.

2.4. Effect of Photoinitiator Concentration and Multiple-Step Laser Exposure

Our study demonstrates that altering the acrylate-to-epoxide ratio in IPN is an effective method for modifying the viscoelastic and thermal behaviors of this material. Additionally, we investigated the impact of photoinitiator (PI) concentration and a multi-step laser scanning technique, which entails exposing the microstructure to the same laser scanning protocol multiple times.[43] Our findings indicate that increasing the PI content in PEGDA: ECC 1:1 allows for the production of IWP structures that are sufficiently polymerized to maintain the desired quality of 3D architecture with less laser exposure applied (**Figure 6a**; See more in Figure S21, Supporting Information). As the PI concentration increases, the optimized laser intensity decreases from 12.9 to 8.6 to 6.5 TW cm^{-2} for 0.5, 1.0 and 2.0 wt.%, respectively (Figures S21 and S22, Supporting Information). Consequently, a rise in T_g of ≈9 K is observed when PI concentration raised from 0.5 to 1.0 wt.%. However, with the further increase to 2.0 wt.%, T_g drops. That indicates 1.0 wt.% as an optimal PI concentration (Figure 6c).

A previous study suggested a double laser scanning technique to minimize the structural defects caused by surface delamination.[43] By comparing in this work single, double, and quadruple exposure steps, we observe that the major difference in the quality of IWP scaffolds is in the laser intensity range of 4.3–6.5 mW (Figure 6b; Figure S23, Supporting Information). The use of multiple exposures in the production of structures results in improved structural quality compared to single-step exposure. This can be attributed to the increased accumulated energy dose

with each exposure step. This, in turn, leads to an increase in T_g with each additional exposure step. When comparing $T_{g,1}$, which corresponds to the linear network of PEGDA, this increase can be directly correlated to the increase in the conversion degree, and is similar to the results obtained in the literature.[43]

We can also see that the mechanical properties of IPN 1:1 with 1 and 2 wt.% PI exhibit notable differences (Figure 6d). For 1 wt.% PI, the structure is compliant and shows a predominantly elastic response. In contrast, the behavior of IPN with 2 wt.% PI shifts more toward PEGDA, displaying a smaller deformation (D_{max}) and a lower elastic recovery range of 50–60%. Multiple exposures have the effect on IPN with 1 wt.% PI, leading to smaller deformations, while no significant changes are observed in IPN 2 wt.% PI, suggesting that the structure reached its maximum mechanical enhancement due to polymerization. These findings highlight the potential for tailoring the properties of IPN and other photocurable polymers through the proposed approaches.

3. Conclusion

This work demonstrates the fabrication and comprehensive characterization of novel interpenetrating polymer network microstructures achieved through Multiphoton Lithography. We combined acrylate- and epoxide-based components to benefit from the properties of each network and their synergistic interactions in the resulting IPNs. Compared to pristine PEGDA, the intricate 3D microstructures fabricated with IPN exhibited improved 3D structural stability. To understand the underlying mechanisms of IPN behavior, the selected IPN microstructures were analyzed by fast scanning calorimetry, tapping mode AFM, force-distance curve AFM and Intermodulation AFM. The combination of these powerful high-resolution methods approached material properties from the microscopic level down to the segmental level and unraveled the mechanical and thermal performance of the IPN with an in-depth understanding of the phenomena discovered therein.

FSC analysis confirmed that all IPN blends were thermally stable. The MPL fabrication parameters affected the conversion degree of the material; thus, the T_g with the highest values are detected for the most exposed samples. However, owing to the interplay of several factors, IPN blends exhibit a complex thermal behavior. These effects include the viscosity difference affecting the mass transport during polymerization, the soft confinement effect of the stiffer ECC on the softer PEGDA network, the dark curing phenomena inherent to epoxide photopolymerization, spinodal phase separation, and the temperature effect. Depending on the IPN mixing ratio and the MPL laser average power and scanning speed, different effect(s) seemed to play a predominant role, resulting in a specific material morphology and behavior. In general, it appears that the dominant effect on the mechanical properties of the structure is the laser scanning velocity, whereas the laser intensity has a major influence on the structural dimensions and thus on the quality of the 3D microstructures. Nevertheless, the thermal behavior is mainly affected by the exposure dose received by the material, and therefore is a result of the interplay between the applied laser intensity and scanning velocity.

The effect of the laser velocity arises from the different kinetics of radical and cationic polymerization. The duration of irradiation directly affects the growth of the PEGDA network, which appears to be the fastest process. Consequently, the slower formation of the ECC network is spatially disturbed to different extents by the already formed acrylate phase. Therefore, varying the laser velocity would be a facile way to achieve IPN materials with various morphologies of PEGDA and ECC phase distributions, leading to different material properties. We believe that changing this MPL fabrication parameter is an easy but powerful tool for tuning IPN thermal and mechanical properties. Moreover, varying of the photoinitiator concentration and utilizing multi-step laser exposure process can lead to enhanced T_g and microstructure apparent stiffness.

At the submicron scale, our IPN materials consist of three distinct phases: a stiffer ECC-rich phase, softer PEGDA-rich phase, and low-density phase. The presence of ECC-rich spherical formations at the microscale appears to be the main difference between the different ratios of IPN materials resulting from spinodal phase separation. This causes different distributions of dissipative energy or stiffness within the materials, which in turn affects the viscoelastic behavior of the IPN at the micron level. All IPN showed approximately ten times higher deformation under load than pristine PEGDA; however, surprisingly, their response was predominantly elastic (80–100%) compared to the plastic nature of PEGDA. Owing to the distinctive ECC-rich phase and tuning of the MPL fabrication parameters, an IPN 1:1 material exhibiting an elastic recovery of 100% was obtained in this work.

In summary, in this study, we succeeded in producing remarkably abundant IPN samples exhibiting Young's moduli ranging from 3 to 4 MPa, good 3D structural stability, and high-to-fully elastic behavior. Such materials are good candidates to fashion the soft microstructures of intricate 3D designs for morphable systems, micro-robotics, and cell engineering.

Our findings encourage the further development and exploration of IPN systems as versatile and easily tunable materials for 3D MPL microstructuring. In addition, our results provide insights into the development of materials and characterization strategies for potential applications in miniaturized multifunctional systems.

4. Experimental Section

Materials: 2,5-Bis[4-[N,N-Bis-[2-(Acetyloxy)Ethyl]Phenyl]-Methylene]-(2E,5E)-Cyclopentanone (BAE) TPP photoinitiator, used to promote radical polymerization, was supplied by GenoSynth GmbH. BAE solution in acetone (500 mg mL^{-1}) was added in studied mixtures. To initiate epoxide ring opening, triarylsulfonium hexafluorophosphate salt (TSHP) was used (Sigma–Aldrich). 3,4-Epoxycyclohexylmethyl-3′,4′-epoxycyclohexane carboxylate (Sigma–Aldrich) was used as a monomer subjected to cationic polymerization. Polyethylene glycol diacrylate with Mn = 575 (Sigma–Aldrich) was used for radical polymerization. The structures of chemicals used in this study are given in Figure S24 (Supporting Information).

To enable the polymerization process, a photoinitiator component was added to the monomers or monomer mixtures. If not mentioned otherwise, BAE was used as a photoinitiator at a concentration of 1 wt.% recalculated based on the amount of PEGDA. To ensure cationic polymerization, 1 wt.% TSHP was added with respect to the epoxide monomer content.

Sample Preparation: Samples were prepared by placing the material between two glass slips using a silicon spacer. No additional treatment

was applied before the fabrication. After fabrication, samples were developed in ethanol for 30 min. For compositions containing epoxide groups, the sample was left for 24 h in the dark and then subjected to the development step.

Multiphoton Lithography: In this study, a Nanofactory from Femtika Ltd. (Vilnius, Lithuania) was utilized for the 3-D processing of materials. The machine was equipped with an erbium-doped fiber laser (Menlo, Germany) emitting at 780 nm, 100 fs pulse duration, and 100 MHz repetition rate. A high-precision 64× immersion oil microscope objective with a numerical aperture (NA) of 1.4 (Plan- Apochromat, Zeiss) was used to focus the laser beam onto the photoresist material. First, arrays of repetitive cubic structures and IWP scaffold units were produced for each studied material formulation with a change in the laser power from 5 to 30 mW in steps of 5 mW. The laser scanning velocities were tested in the range of 1000–10 000 µm s^{-1} with a step of 2250 µm s^{-1}. All prints were scripted with the hatching and slicing set to 0.2 and 0.5 µm, respectively, to ensure continuous polymer formation. All the structures were printed from glass onto the photoresist.

Selected fabrication parameters were applied to the photoresists directly deposited onto calorimetric chips to further study their thermal properties. An extralong distance 20× air objective (Plan-Fluor, Nikon) with 0.45 NA was used. A 100 × 100 μm^2 structure was printed directly on the active area of the chip. Microfabrication was performed such that two slicing steps were applied to ensure similar thicknesses for all the produced samples. A cubic structure array was produced as described above to study the influence of fabrication parameters on viscoelastic properties using AFM.

Laser intensity was determined as described elsewhere.[44] using the following equation:

$$I = \frac{2TP_{peak}}{\pi r^2} \quad (1)$$

where T is the transmittance of the focusing objective at 780 nm, P_{peak} is the peak power, and r is the Airy radius. T was taken from the supplier datasheet as 0.78 and 0.86 for oil immersion (1.4 NA) and air objectives (0.45 NA). The peak power and Airy radius were calculated according to the following equations:

$$P_{peak} = \frac{P_{ave}}{R\tau};\ r = \frac{0.61\lambda}{NA} \quad (2)$$

Fast Scanning Calorimetry: Fast Scanning Calorimetry was employed to study the thermal properties (glass transition behavior) of the MPL microstructures. A power compensated DSC Mettler Toledo Flash DSC1.[45] was used in this work. It was based on non-adiabatic chip calorimetry, employing a UFS1-sensor,[46] based on Micro-Electro-Mechanical System with two separate calorimeters (sample and reference side). It allows for heating rates in the range of $\dot{T} = 0.5$–40 000 K s^{-1} due to the low signal time constant of the device (1 ms) and low mass of the sample.[47] The MPL microstructure was fabricated directly on the active heating area of the sample side, which ensures the structure integrity, as well as a good thermal contact of the material with the sensor. To minimize thermal lags the approximate dimensions of the print were 400 × 400 μm^2, which was well below the edge values of the device. A nitrogen flow of 20 mL min^{-1} was used to purge the measurement cell during the experiment. Conditioning and correction procedures given by the manufacturer were applied prior to the measurement. The measurements were carried out in a temperature range of 298–500 K. The glass transition temperature was extracted from the peak maxima of the first derivative of the heat flow.

Atomic Force Microscopy: An MFP-3D microscope (Oxford Instruments Asylum Research, Santa Barbara, CA, USA) was used for atomic force microscopy measurements. Three AFM modes were applied: tapping mode, force distance curves, and intermodulation AFM. An array of cubic 3D structures (50 × 50 × 10 μm^3) was fabricated with 1.4NA objective varying average laser power from 10 to 25 mW (2.2–12.9 TW cm^{-2}) and laser velocities between 1000 and 10 000 µm s^{-1}.

Force–distance curve AFM measurements were performed using a µMasch HQ:NSC35/Cr–Au cantilever C (NanoandMore, Wetzlar, Germany) with a resonance frequency f_0 of 110 kHz and a spring constant k_c of 3.4 N m^{-1}. To evaluate the mechanical properties of PEGDA and PEGDA:ECC (7:3 and 1:1), an array of 16 cubic microstructures (50 × 50 × 10 μm^3) with alternating laser powers ranging from 10 to 25 mW in four steps and laser velocities from 1000 to 10 000 µm s^{-1} in four steps was fabricated with the MPL. FDCs were recorded at 1 Hz with a maximum applied force F_{max} of 68 nN. To make the results comparable for different materials, the maximum load F_{max} was kept the same for all measurements. Each measurement consisted of 8 × 8 FDCs on an 8 × 8 μm^2 area of the microstructure surface. The curves of each force volume were averaged and evaluated for maximal deformation D_{max}, plastic deformation,[39] and elastic recovery. (See Supporting Information for details). Measurements, shown in Figure 6d, were performed using a PP NCHR (Nanosensors) with a spring constant k_c of 43 N m^{-1}. 6 × 6 FDCs were recorded at 1 Hz with a maximum applied force F_{max} of 0.86 µN and subsequently averaged.

ImAFM amplitude-dependent force spectroscopy was performed using an AFM equipped with a µMasch HQ:NSC15/Cr-Au cantilever (NanoandMore, Wetzlar, Germany) with a resonance frequency f_0 = 252 kHz and a spring constant of k_c = 22.2 N m^{-1}. Each measurement consisted of a force volume of 256 × 256 ADFS curves on a 2 × 2 μm^2 area. ADFS curves were evaluated for stiffness k_{eff}, maximum attractive force F_{attr} and dissipative energy E_{dis} as described elsewhere.[30,40] Tapping mode images were edited with WSXM.[48] Cubic samples fabricated at two different laser powers and two different scan velocities, analogue to the investigation of the thermal properties were investigated: 10 mW, 1000 µm s^{-1}; 20 mW, 7000 µm s^{-1} and 20 mW, 1000 µm s^{-1}.

Supporting Information

Supporting Information is available from the Wiley Online Library or from the author.

Acknowledgements

The authors acknowledge funding by the Deutsche Forschungsgemeinschaft (DFG, German Research Foundation) under grant number 457594480.

Open access funding enabled and organized by Projekt DEAL.

Conflict of Interest

The authors declare no conflict of interest.

Author Contributions

D.S. and P.S. contributed equally to this work. D.S. performed data curation (equal), formal analysis (equal), validation, wrote the original draft (equal). P.S. performed data curation (equal), formal analysis (equal), validation, wrote the original draft (equal). Z.T. performed data curation (supporting), experimental design (supporting). H.S. wrote, review and edit the final manuscript (supporting). I.T. performed conceptualization (lead), methodology, supervision, wrote the original draft (equal), review and edit the final manuscript (lead).

Data Availability Statement

The data that support the findings of this study are available from the corresponding author upon reasonable request.

Keywords

atomic force microscopy, fast scanning calorimetry, intermodulation AFM, interpenetrating polymer network, multiphoton lithography

Received: November 17, 2023
Revised: April 9, 2024
Published online:

[1] M. Farsari, B. N. Chichkov, *Nat. Photonics* **2009**, *3*, 450.
[2] I. Topolniak, A. M. Elert, X. Knigge, G. C. Ciftci, J. Radnik, H. Sturm, *Adv. Mater.* **2022**, *34*, 2109509.
[3] J. Maciulaitis, S. Rekštytė, M. Bratchikov, R. Gudas, M. Malinauskas, A. Pockevicius, A. Usas, A. Rimkunas, V. Jankauskaite, V. Grigaliunas, R. Maciulaitis, *Appl. Surf. Sci.* **2019**, *487*, 692.
[4] Z. Tavasolyzadeh, P. Tang, M. Benjamin Hahn, G. Hweidi, N. Nordholt, R. Haag, H. Sturm, I. Topolniak, *Small* **2024**, *20*, 2309394.
[5] A. Accardo, M.-C. Blatché, R. Courson, I. Loubinoux, C. Thibault, L. Malaquin, C. Vieu, *Small* **2017**, *13*, 1700621.
[6] F. Rajabasadi, L. Schwarz, M. Medina-Sánchez, O. G. Schmidt, *Prog. Mater. Sci.* **2021**, *120*, 100808.
[7] P. Cabanach, A. Pena-Francesch, D. Sheehan, U. Bozuyuk, O. Yasa, S. Borros, M. Sitti, *Adv. Mater.* **2020**, *32*, 2003013.
[8] R. Houbertz, P. Declerck, S. Passinger, A. Ovsianikov, J. Serbin, B. N. Chichkov, *physica status solidi a* **2007**, *204*, 3662.
[9] I. Sakellari, E. Kabouraki, D. Karanikolopoulos, S. Droulias, M. Farsari, P. Loukakos, M. Vamvakaki, D. Gray, *Nanoscale Adv.* **2019**, *1*, 3413.
[10] M. Malinauskas, H. Gilbergs, A. Žukauskas, V. Purlys, D. Paipulas, R. Gadonas, *J. Opt.* **2010**, *12*, 035204.
[11] L. Siegle, S. Ristok, H. Giessen, *Opt. Express* **2023**, *31*, 4179.
[12] I. V. A. K. Reddy, A. Bertoncini, C. Liberale, *Optica* **2022**, *9*, 645.
[13] L. Amato, Y. Gu, N. Bellini, S. M. Eaton, G. Cerullo, R. Osellame, *Lab Chip* **2012**, *12*, 1135.
[14] Y.-J. Liu, J.-Y. Yang, Y.-M. Nie, C.-H. Lu, E. D. Huang, C.-S. Shin, P. Baldeck, C.-L. Lin, *Microfluid. Nanofluidics* **2015**, *18*, 427.
[15] S. Maruo, K. Ikuta, H. Korogi, *Appl. Phys. Lett.* **2003**, *82*, 133.
[16] S. Maruo, K. Ikuta, H. Korogi, *J. Microelectromech. Syst.* **2003**, *12*, 533.
[17] A. Xomalis, O. Tsilipakos, M. Manousidaki, P. D.e G. Busquets, G. Kenanakis, S. Tzortzakis, M. Farsari, C. M. Soukoulis, E. N. Economou, M. Kafesaki, *ACS Appl. Opt. Mater.* **2023**, *1*, 10.
[18] G. Flamourakis, I. Spanos, Z. Vangelatos, P. Manganas, L. Papadimitriou, C. Grigoropoulos, A. Ranella, M. Farsari, *Macromol. Mater. Eng.* **2020**, *305*, 2000238.
[19] C. Liao, A. Wuethrich, M. Trau, *Appl. Mater. Today* **2020**, *19*, 100635.
[20] K. Dean, W. D. Cook, *Macromol.* **2002**, *35*, 7942.
[21] C. Decker, N. T. Viet, D. Decker, E. Weber-Koehl, *Polymer* **2001**, *42*, 5531.
[22] C. Decker, N. T. Viet, P. Thi, *Polym. Int.* **2001**, *50*, 986.
[23] J. P. Fouassier, J. Lalevée, *Polymers* **2014**, *6*, 2588.
[24] L. H. Sperling, In *Interpenetrating Polymer Networks*, American Chemical Society, Washington, D.C **1994**.
[25] R. Raveendran, C. P. Sharma, In *Micro- and Nano-structured Interpenetrating Polymer Networks*, John Wiley & Sons, Inc **2016**, pp. 383–397.
[26] N. C. Murillo, P. Szymoniak, G. J. Smales, H. Sturm, A. Schönhals, *ACS Appl. Opt. Mater.* **2021**, *3*, 6572.
[27] M. Belqat, X. Wu, L. P. C. Gomez, J.-P. Malval, S. Dominici, B. Leuschel, A. Spangenberg, K. Mougin, *Addit. Manuf.* **2021**, *47*, 102232.
[28] B. Buchroithner, D. Hartmann, S. Mayr, Y. J. Oh, D. Sivun, A. Karner, B. Buchegger, T. Griesser, P. Hinterdorfer, T. A. Klar, J. Jacak, *Nanoscale Adv.* **2020**, *2*, 2422.
[29] Z. Hajjarian, H. T. Nia, S. Ahn, A. J. Grodzinsky, R. K. Jain, S. K. Nadkarni, *Sci. Rep.* **2016**, *6*, 37949.
[30] G. Z. Khorasani, D. Silbernagl, D. Platz, H. Sturm, *Polymers* **2019**, *11*, 235.
[31] D. Platz, D. Forchheimer, E. A. Tholén, D. B. Haviland, *Nat. Commun.* **2013**, *4*, 1360.
[32] J. C. Dinis, T. F. Morais, P. H. J. Amorim, R. B. Ruben, H. A. Almeida, P. N. Inforçati, P. J. Bártolo, J. V. L. Silva, *Procedia Technol.* **2014**, *16*, 1542.
[33] D. Gonzalez-Hernandez, B. Sanchez-Padilla, D. Gailevičius, S. C. Thodika, S. Juodkazis, E. Brasselet, M. Malinauskas, *Adv. Opt. Mater.* **2023**, *11*, 2300258.
[34] S. Rekštytė, T. Jonavičius, D. Gailevičius, M. Malinauskas, V. Mizeikis, E. G. Gamaly, S. Juodkazis, *Adv. Opt. Mater.* **2016**, *4*, 1209.
[35] E. Skliutas, M. Lebedevaite, E. A. Kabouraki, T. Baldacchini, J. Ostrauskaite, M. Vamvakaki, M. Farsari, S. Juodkazis, M. Malinauskas, *Nanophotonics* **2021**, *10*, 1211.
[36] B. Golaz, V. Michaud, Y. Leterrier, J. A. E. Månson, *Polymer* **2012**, *53*, 2038.
[37] K. Kunal, C. G. Robertson, S. Pawlus, S. F. Hahn, A. P. Sokolov, *Macromol* **2008**, *41*, 7232.
[38] B. Cappella, G. Dietler, *Surf. Sci. Rep.* **1999**, *34*, 1
[39] M. Dudziak, I. Topolniak, D. Silbernagl, K. Altmann, H. Sturm, *Nanomaterials* **2021**, *11*, 3285.
[40] D. Silbernagl, M. Ghasem Zadeh Khorasani, N. Cano Murillo, A. M. Elert, H. Sturm, *Beilstein J. Nanotechnol.* **2021**, *12*, 58.
[41] M. L. Torres-Mapa, M. Singh, O. Simon, J. L. Mapa, M. Machida, A. Günther, B. Roth, D. Heinemann, M. Terakawa, A. Heisterkamp, *Sensors* **2019**, *19*, 4333.
[42] W.-F. Su, Y.-C. Fu, W.-P. Pan, *Thermochim. Acta* **2002**, *392–393*, 385.
[43] J. Lee, S. J. Park, S. C. Han, P. Prabhakaran, C. W. Ha, *Mater. Des.* **2023**, *235*, 112389.
[44] E. Skliutas, D. Samsonas, A. Čiburys, L. Kontenis, D. Gailevičius, J. Berzinš, D. Narbutis, V. Jukna, M. Vengris, S. Juodkazis, M. Malinauskas, *Virtual Phys. Prototyp.* **2023**, *18*, e2228324.
[45] V. Mathot, M. Pyda, T. Pijpers, G. Vanden Poel, E. van de Kerkhof, S. van Herwaarden, F. van Herwaarden, A. Leenaers, *Thermochim. Acta* **2011**, *522*, 36.
[46] S. van Herwaarden, E. Iervolino, F. van Herwaarden, T. Wijffels, A. Leenaers, V. Mathot, *Thermochim. Acta* **2011**, *522*, 46.
[47] J. E. K. Schawe, *J. Therm. Anal. Calorim.* **2014**, *116*, 1165.
[48] I. Horcas, R. Fernández, J. M. Gómez-Rodríguez, J. Colchero, J. Gómez-Herrero, A. M. Baro, *Rev. Sci. Instrum.* **2007**, *78*, 013705.